Earth and Planetary Science Letters 307 (2011) 83–93

Contents lists available at ScienceDirect

Earth and Planetary Science Letters

journal homepage: www.elsevier.com/locate/epsl

West Antarctic Ice Sheet elevations in the Ohio Range: Geologic constraints and ice sheet modeling prior to the last highstand

Robert P. Ackert Jr. [a,*], Sujoy Mukhopadhyay [a], David Pollard [b], Robert M. DeConto [c], Aaron E. Putnam [d], Harold W. Borns Jr. [d]

[a] Department of Earth and Planetary Sciences, Harvard University, Cambridge, MA 02138, United States
[b] Earth and Environmental Systems Institute, Pennsylvania State University, University Park, PA 16802, United States
[c] Department of Geosciences, University of Massachusetts, Amherst, MA 01003, United States
[d] Climate Change Institute, University of Maine, Orono, ME 04469, United States

ARTICLE INFO

Article history:
Received 4 December 2010
Received in revised form 1 April 2011
Accepted 14 April 2011
Available online 14 May 2011

Editor: P. DeMenocal

Keywords:
WAIS
^{3}He
^{10}Be
exposure dating
marine ice sheet
ice sheet model

ABSTRACT

Knowledge of the timing and extent of past West Antarctic Ice Sheet (WAIS) elevation changes provides insight to the WAIS response to sea level and climate forcing, as well as constraints for ice sheet models. Trimlines and erratics indicate that maximum ice elevation at the Ohio Range, located near the WAIS divide, was 125 m above the present ice surface and was reached at ~10 ka. However, ^{3}He and ^{10}Be exposure ages of most granitic erratics and supra-glacial boulders in adjacent blue ice areas are older than the last highstand and provide constraints on earlier interior WAIS elevation changes. Although diffusive loss of ^{3}He occurs in quartz, an excellent correlation between ^{3}He and ^{10}Be concentrations in samples up to 400 ka is observed in the Ohio Range, demonstrating the utility of ^{3}He measurements in Antarctic quartz. The correlation is used to calculate "equivalent ^{10}Be exposure ages" from the larger ^{3}He data set. The exposure ages occur in distinct clusters 10–20 ka, 70–80 ka, 130–140 ka and 180–190 ka that we relate to pulses in the emergence of englacial debris in localized blue ice ablation areas. A combined ice sheet/ice shelf model predicts that WAIS elevations near the Ohio Range have varied only ~125 m over the last 200 kyr with highstands at ~10 ka and ~130 ka, in good agreement with observations of trimlines and peaks in the exposure age distribution at the Ohio Range. In the model, interior WAIS elevations are controlled by the interaction of accumulation rates and ice dynamics related to ice sheet/ocean interactions at the grounding line. WAIS highstands occur early in interglacial periods during intervals of warmer temperatures and high accumulation rates, prior to the arrival of a wave of thinning. We hypothesize that the correspondence of rising regional WAIS elevation with debris pulses relates to increased ice (debris) flux and ablation in the local blue ice areas resulting from the warmer temperatures. The occurrence of clasts with exposure ages up to 200 ka on the WAIS surface indicates elevation changes near the Ohio Range were limited in extent during stage 5e. The geologic observations, combined with model results, place constraints on WAIS geometry during stage 5e and limit the WAIS contribution to the higher sea levels observed during the last interglacial to ~3 m.

1. Introduction

Over the last decade, glacial geologic and ice core data combined with ice sheet models indicate that the WAIS did not approach equilibrium during the last glacial maximum (LGM) (Ackert et al., 1999, 2007; Price et al., 2007; Waddington et al., 2005). Changes on the periphery of the WAIS, grounded on the continental shelf (Anderson et al., 2002) have been driven primarily by ice sheet/ocean interactions. In contrast, the interior of the ice sheet is thought to respond primarily to changes in accumulation rates that are largely controlled by temperature e.g. (Alley and Whillans, 1984; Steig et al., 2001). Thus, during the LGM (~20 ka), when the WAIS was at maximum extent in the Ross and Weddell Seas (Anderson et al., 2002; Brambati et al., 2002; Licht et al., 1996; Shipp et al., 1999), surface elevations in the interior of the ice sheet were probably no higher than present, and possibly lower.

Maximum interior WAIS surface elevations did not occur until the early Holocene at ~10 ka (Ackert et al., 1999, 2007). Ice sheet models indicate early interglacial highstands are the result of increased accumulation (maximum temperatures) over cold, slowly flowing ice formed during the glacial maximum, prior to the arrival of a wave of thinning that propagated inland following grounding line retreat (Ackert et al., 1999, 2007; Steig et al., 2001). However, the history of interior WAIS fluctuations prior to the last highstand is largely unknown. Thus, WAIS contributions to global sea level and ice sheet model simulations prior to the LGM remain unconstrained.

* Corresponding author. Tel.: +1 617 496 6449.
E-mail address: rackert@fas.harvard.edu (R.P. Ackert).

0012-821X/$ – see front matter © 2011 Elsevier B.V. All rights reserved.
doi:10.1016/j.epsl.2011.04.015

Surface exposure dating of glacial boulders provides a potential source of information on pre-LGM WAIS fluctuations. However, surface exposure ages from WAIS moraines or drift sheets beyond the LGM margin tend to scatter widely (Ackert et al., 1999; Brook et al., 1995; Todd et al., 2010). Invariably, boulders with older exposure ages are also found within LGM moraines and drift in Antarctica (Ackert et al., 2007; Bentley et al., 2010; Brook et al., 1995; Mackintosh et al., 2007; Stone et al., 2003; Todd et al., 2010). Unlike the youngest ages associated with the most recent down draw, the older exposure ages do not show clear relationships with elevation. These older exposure ages are attributed to prior exposure of the samples and typically are not further considered. Here we show that in the Ohio Range, useful chronologic information on WAIS history is contained in the probability distributions of the older exposure ages.

The Ohio Range (85°S; 114°W) is an east–west trending escarpment in the Horlick Mountains near the WAIS divide that separates the East and West Antarctic Ice Sheets (Fig. 1A). The escarpment exposes granitic basement rocks, capped by Permian sandstones and tillites. The granite bedrock is deeply weathered with pits typically greater than 10 cm and occasionally up to meter scale. Rising 500 m above the surface of the WAIS (~1500 m), the Ohio Range diverts flow from the thicker EAIS into the WAIS (Fig. 1B). Although some ice from the Buckeye Table flows over the escarpment, ice elevation at the base of the escarpment is determined by the regional WAIS elevation (Fig. 1B and C). Ridges projecting north from the escarpment restrict the accumulation of windblown snow carried by the prevailing easterly winds on their western sides. As a result, local ablation (blue ice) areas occur in the lee of Discovery Ridge and Darling Ridge (Fig. 1B). Extensive supraglacial debris and ice-cored moraines in the blue ice areas (Fig. 2) attest to the stability of the ablation areas, while moraines and erratics on the adjacent ice-free parts of the escarpment and nunataks record higher ice levels (Mercer, 1963). Thus, the Ohio Range Escarpment is well situated to record changes in regional WAIS elevations.

The highest recorded WAIS elevation is marked by a trimline 125 m above the present WAIS surface. Exposure dating of erratics at the trimline indicates the last highstand ended 10.8 ± 1.0 ka (Ackert et al., 2007). However, almost all of the sampled erratics from both the ice-free bedrock and the blue ice have ^{3}He or ^{10}Be exposure ages significantly older than the last highstand. Here we compare the exposure age distribution of erratic clasts and boulders from the Ohio Range Escarpment and ice-cored moraines on the adjacent WAIS surface with ice core temperature records and an ice sheet model simulation of the WAIS elevation history in order to constrain interior WAIS surface elevations prior to the LGM.

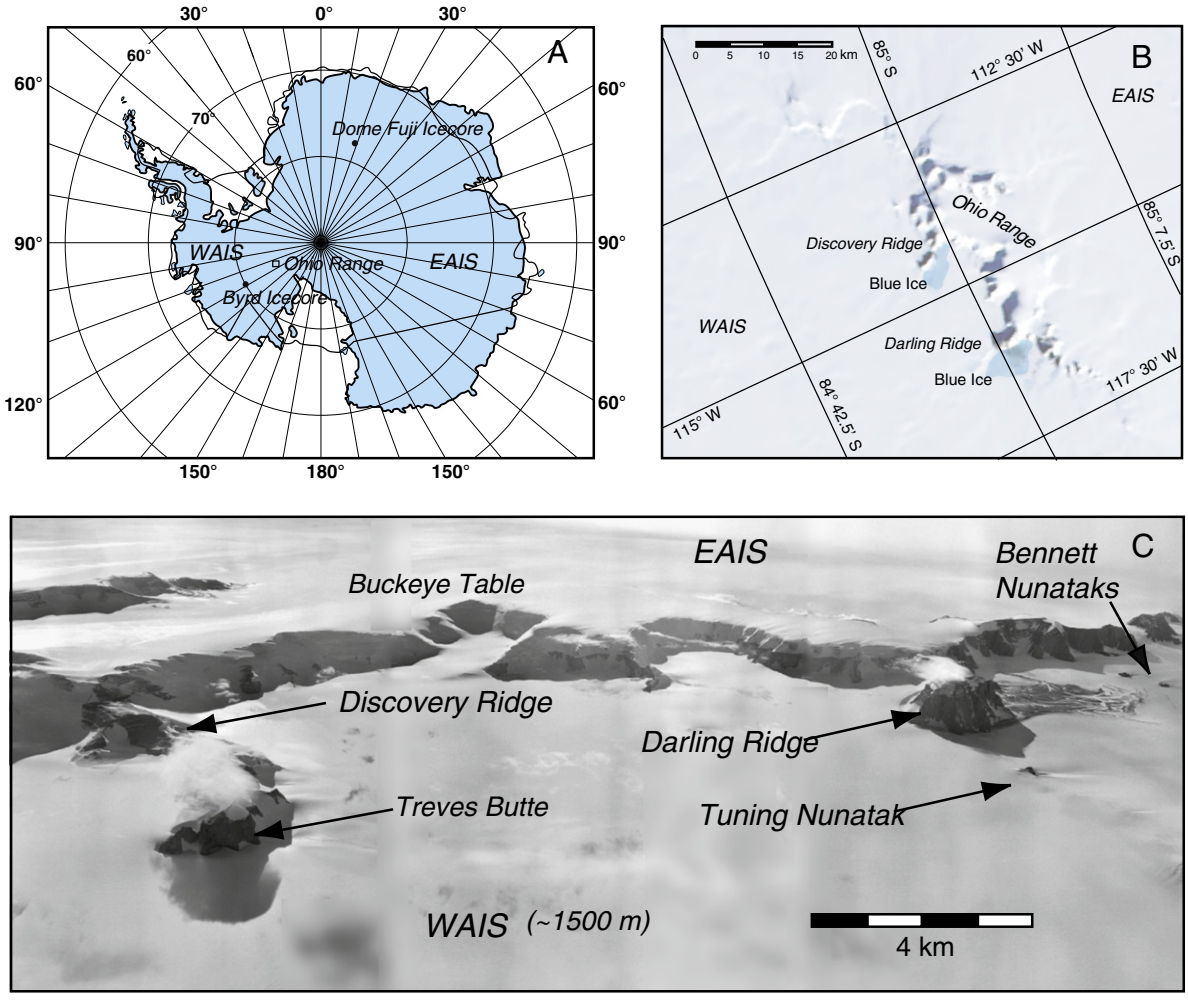

Fig. 1. A) Location map of Antarctica. The box labeled Ohio Range corresponds to location of Fig. 1B. B) MOA satellite image of the Ohio Range. Blue ice areas indicating local net ablation are visible to the west of Discovery and Darling Ridge. C) Mosaic of oblique aerial photographs showing the Ohio Range Escarpment. Extensive ice-cored moraines are visible west of Darling Ridge. Ice-cored moraines also occur in the lee of Discovery Ridge and Treves Butte. There, a broad curving moraine marks the convergence of WAIS ice flowing toward the Ohio Range Escarpment west of Treves Butte with limited local ice flowing westward thorough the gap between Discovery Ridge and Treves Butte.

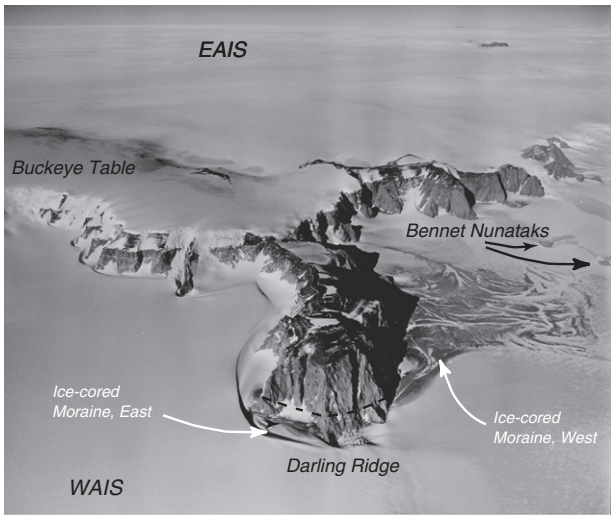

Fig. 2. Oblique aerial photograph showing the local blue ice ablation area and ice-cored moraines in the lee on the west side of Darling Ridge. Another ice-cored lateral moraine occurs in the wind scoop that creates a small ablation area on the east side of Darling Ridge. In contrast to the other areas of ice-cored moraine, the debris composing this moraine appears to be sourced from the nearby cliffs of the escarpment. Data from the East Darling Ridge Moraine is not included in Fig. 3B or Fig. 5.

2. Material and methods

2.1. Sample collection

Descriptions of the sampling procedures, and analytical methods appear in Ackert et al. (2007) that highlighted the youngest exposure ages from the most recent WAIS highstand at the Ohio Range Escarpment. Thus, we only include a brief summary here. A trim line demarking the past vertical extent of the WAIS was mapped from distribution of glacial deposits, erosional features, and the relative weathering of the underlying bedrock. We sampled erratics on transects from the WAIS ice margin to the peaks of several nunataks within the blue ice areas and at the trimline on Discovery Ridge and Darling Ridge. We also sampled erratics from three ice-cored moraines on the WAIS surface near Discovery and Darling Ridge (Fig. 2). The bulk of the supra-glacial debris in these locations is carried by ice flowing over the Buckeye Table (Fig. 1C) to the east and west that is deflected into the blue ice areas at the base of the escarpment by the WAIS.

In the Ohio Range, extremely low subaerial erosion rates and non-erosive cold-based ice results in the pervasive occurrence of bedrock and regolith with long exposure to cosmic radiation, and granite erratics and bedrock with cavernously weathered surfaces are common. As our primary goal was constraining the last WAIS highstand, we focused on sampling fresh-looking clasts with sharp angular edges that have undergone negligible erosion. In practice, the surfaces of the clasts ranged from completely unweathered, to slightly wind-abraded and etched. We note that these sampling criteria are biased toward boulders with younger exposure ages and that older boulders are under-represented. Differences in crystal-size and mineralogy were used to differentiate erratics from locally derived clasts in order to avoid sampling local rockfall.

The predominance of granite erratics makes quartz the preferred target mineral for cosmogenic nuclide measurements. At Antarctic temperatures, He diffusion rates in quartz are low enough that significant quantities of cosmogenic ^{3}He are retained for at least 100 kyr (Brook and Kurz, 1993) and can be used to calculate "apparent" exposure ages. We use the term apparent to indicate that the ^{3}He exposure ages in quartz are minimums, due to possible diffusive loss of cosmogenic ^{3}He. In addition, measurement of ^{3}He provides an efficient way to screen for prior exposure.

2.2. ^{3}He measurements

Helium isotopes in quartz separates hand-picked from 60 granite boulders and clasts from the Ohio Range were measured on the Nu Noblesse mass spectrometer in the Noble Gas Laboratory at Harvard University (Table 1). Between 20 and 100 mg of quartz were loaded into Ta foil boats and heated to 1200 °C in a resistance furnace connected to a fully automated extraction line. The evolved gasses were sequentially exposed to a hot and cold SAES getter and then trapped onto a cryogenic cold-finger at 12 K. Helium was released from the trap at 32 K and inlet into the mass spectrometer. Helium isotopic ratios and concentrations were determined by normalizing to a standard with a ^{3}He/^{4}He of 8.8 R_A (where R_A is the ^{3}He/^{4}He ratio normalized to the atmospheric ratio of 1.39×10^{-6} that was prepared at Harvard (HH3)). ^{4}He was measured using a Faraday cup and ^{3}He was measured using a discrete dynode multiplier operating in pulse counting mode.

Replicates measurements were made on 19 samples. In most cases, the ^{3}He concentrations fall within the 2σ analytical uncertainties. In four samples, the variability of ^{3}He concentrations is larger, between 6 and 16%, probably reflecting heterogeneous ^{3}He retention. For samples that were replicated, the arithmetic mean and standard deviation of the ^{3}He concentrations were used for calculating exposure ages and the uncertainty on the exposure age. In two samples the measured ^{3}He concentrations are significantly different. The cause of this variability is unclear and these data were not used. The apparent ^{3}He exposure ages were calculated by scaling the production rate of 120 ± 9.4 atoms/g/yr (olivine) (Goehring et al., 2010) to quartz using the elemental production rates of Masarik and Reedy (1996) and the Antarctic altitude scaling of Stone (2000), which is based on the current atmospheric pressure field over Antarctica.

2.3. ^{10}Be measurements

^{10}Be was measured in a subset of 14 samples representative of the modal peaks in the apparent ^{3}He age distribution (Table 2). We use the ^{10}Be measurements to calibrate the apparent ^{3}He exposure ages (Section 3). Techniques for the extraction of ^{10}Be from quartz and its measurement by AMS are well established. Samples were prepared at Oregon State University following methods of Licciardi (2000) slightly modified by Goehring (2006). AMS measurements were carried out at the PRIME lab AMS facility, Purdue University. ^{10}Be exposure ages were determined using the CRONUS web based calculator (Balco et al., 2008), utilizing a ^{10}Be decay constant of $5.10\pm0.26\times10^{-7}$ yr^{-1} (Nishiizumi et al., 2007) and a sea level high latitude production rate of 4.49 ± 0.39 atoms/g/yr. The calculator also utilizes the Stone (2000) scaling. We note that recent calibrations of the ^{10}Be production rates from New Zealand and North America are significantly lower (Putnam et al., 2010; Balco et al., 2009) and would increase our exposure ages by ~14%. However, it is currently not known whether these new calibrations are applicable to Antarctica.

3. Results

3.1. Distribution of apparent ^{3}He exposure ages

Histograms and probability density functions (PDF) of the apparent ^{3}He exposure age distributions from the Ohio Range are shown in Fig. 3. As there are insufficient samples with exposure ages >200 ka to determine a meaningful PDF beyond this age, the figure is truncated a 200 ka. Only the analytical uncertainties are used to generate the PDF because systematic production rate and scaling uncertainties have the effect of "smearing" the PDF and obscuring the actual clustering of the exposure ages. Systematic errors cause all ages to shift proportionately in

Table 1
Helium isotope data and exposure ages of granite erratics from the Ohio Range.

Sample	Elevation (m)	Latitude S	Longitude W	Depth (cm)	^{4}He (atom/g$\times 10^{12}$)	^{3}He/^{4}He (R/Ra)	^{3}He cosmo (atom/g$\times 10^6$)	Age (ka)
Tuning Nunatak								
OTN-05-001-1	1539	84° 43.88′	115° 57.955′	2	79.41 ± 0.0009	0.60 ± 0.01	64.88 ± 0.72	104.5 ± 1.2
OTN-05-001-2a	1539	84° 43.88′	115° 57.955′	2	3.50 ± 0.0009	7.07 ± 0.08	34.23 ± 0.40	55.1 ± 0.6
OTN-05-001-2b	1539	84° 43.88′	115° 57.955′	2	41.89 ± 0.0072	0.68 ± 0.01	39.00 ± 0.49	62.8 ± 0.8
OTN-05-001							*Mean*	*112.1 ± 0.8*
OTN-05-019-1	1539	84° 43.88′	115° 57.902′	3	61.47 ± 0.0050	0.34 ± 0.00	28.74 ± 0.35	*47.1 ± 0.6*
OTN-05-019-2a	1540	84° 43.88′	115° 57.902′	3	4.62 ± 0.0014	1.69 ± 0.03	10.77 ± 0.18	17.6 ± 0.3
OTN-05-019-2b	1540	84° 43.88′	115° 57.902′	3	198.02 ± 0.0519	0.07 ± 0.00	17.56 ± 0.26	28.7 ± 0.4
OTN-05-019								*46.7 ± 0.4*
OTN-05-021-1	1539	84° 43.88′	115° 57.902′	2	111.40 ± 0.0034	0.48 ± 0.01	72.56 ± 1.09	*116.9 ± 1.8*
OTN-05-022-1	1480	84° 43.827′	115° 58.194′	3	7.35 ± 0.0005	7.02 ± 0.08	71.32 ± 0.84	122.4 ± 1.4
OTN-05-023-1	1480	84° 43.827′	115° 58.194′	2	9.63 ± 0.0005	17.28 ± 0.18	230.24 ± 2.45	388.6 ± 4.1
OTN-05-024-1	1514	84° 43.877′	115° 57.489′	3	32.88 ± 0.0011	2.48 ± 0.03	112.41 ± 1.53	187.8 ± 2.6
OTN-05-024-2	1514	84° 43.877′	115° 57.489′	3	7.86 ± 0.0004	11.03 ± 0.13	119.85 ± 1.44	200.3 ± 2.4
OTN-05-024							*Mean*	*194.4 ± 1.8*
OTN-05-115-1	1539	84° 43.883′	115° 57.852′	2	62.80 ± 0.0008	0.62 ± 0.01	53.19 ± 0.59	*85.7 ± 1.0*
OTN-05-115-2	1539	84° 43.883′	115° 57.852′	2	49.28 ± 0.0077	0.82 ± 0.01	55.52 ± 0.76	89.4 ± 1.2
OTN-05-115								87.1 ± 0.8
OTN-05-118-1	1492	84° 43.884′	115° 58.129′	2	53.46 ± 0.0065	1.28 ± 0.04	94.49 ± 2.62	158.0 ± 4.4
OTN-05-118-2	1492	84° 43.884′	115° 58.129′	2	5.49 ± 0.0005	14.95 ± 0.34	113.62 ± 2.56	189.9 ± 4.3
OTN-05-120-1	1515	84° 43.86′	115° 58.086′	3	7.37 ± 0.0019	2.82 ± 0.13	28.68 ± 1.29	*47.9 ± 2.2*
OTN-05-120-2	1515	84° 43.86′	115° 58.086′	3	33.88 ± 0.0021	0.55 ± 0.02	25.60 ± 1.03	42.7 ± 1.7
OTN-05-120							*Mean*	44.7 ± 1.3
OTN-05-201-1	1539	84° 43.883′	115° 57.956′	2	20.54 ± 0.0010	1.02 ± 0.02	28.69 ± 0.47	*46.2 ± 0.8*
OTN-05-202-1	1470	84° 43.821′	115° 58.265′	3	15.48 ± 0.0005	9.17 ± 0.12	196.28 ± 2.59	339.6 ± 4.5
OTN-05-202-2	1470	84° 43.821′	115° 58.265′	3	13.77 ± 0.0005	9.12 ± 0.11	173.67 ± 2.03	300.5 ± 3.5
OBN-05-202-3	1470	84° 43.821′	115° 58.265′	3	7.89 ± 0.0003	15.46 ± 0.18	168.68 ± 1.95	291.9 ± 3.4
OTN-05-202-4	1470	84° 43.821′	115° 58.265′	3	24.63 ± 0.023	5.758 ± 0.077	196.08 ± 2.63	339.3 ± 4.6
Bennett Nunataks								311.9 ± 1.9
OBN-05-025-1	1465	84° 47.254′	116° 23.718′	2.5	5.24 ± 0.0003	8.86 ± 0.13	64.26 ± 0.96	110.7 ± 1.7
OBN-05-026-1	1491	84° 47.23′	116° 23.958′	2	9.29 ± 0.0004	9.44 ± 0.11	121.24 ± 1.37	202.8 ± 2.3
OBN-05-028A-1	1488	84° 47.23′	116° 23.958′	2	10.99 ± 0.0061	0.75 ± 0.02	11.36 ± 0.35	19.0 ± 0.6
OBN-05-028A-2	1488	84° 47.23′	116° 23.958′	2	2.22 ± 0.0004	4.19 ± 0.27	12.87 ± 0.83	21.6 ± 1.4
OBN-05-028A							*Mean*	19.4 ± 0.5
OBN-05-028B-1	1488	84° 47.23′	116° 23.958′	3	5.76 ± 0.0004	2.19 ± 0.04	17.37 ± 0.35	29.6 ± 0.6
OBN-05-029-1	1483	84° 47.231′	116° 23.865′	3	5.43 ± 0.0003	38.29 ± 0.50	287.63 ± 3.72	492.6 ± 6.4
OBN-05-036-1	1451	84° 46.795′	116° 28.29′	3	5.47 ± 0.0003	17.91 ± 0.19	135.62 ± 1.46	238.3 ± 2.6
OBN-05-037-1	1451	84° 46.795′	116° 28.29′	2	10.55 ± 0.0021	3.43 ± 0.04	49.91 ± 0.61	86.2 ± 1.0
OBN-05_038-1	1448	84° 46.793′	116° 28.241′	3.5	15.04 ± 0.0005	3.28 ± 0.04	68.18 ± 0.84	121.1 ± 1.5
OBN-05-039-1	1448	84° 46.793′	116° 28.241′	3	5.98 ± 0.0004	14.12 ± 0.16	116.85 ± 1.36	205.8 ± 2.4
OBN-05-067-1	1417	84° 46.826′	116° 28.108′	2.5	10.33 ± 0.0006	2.21 ± 0.04	31.49 ± 0.50	56.4 ± 0.9
OBN-05-121-1	1426	84° 47.292′	116° 23.39′	2.5	21.78 ± 0.0010	1.70 ± 0.02	51.11 ± 0.72	90.8 ± 1.3
OBN-05-122-1	1410	84° 47.305′	116° 23.397′	2	13.93 ± 0.0008	0.50 ± 0.01	9.45 ± 0.24	16.9 ± 0.4
OBN-05-122-2	*1410*	*84° 47.305′*	*116° 23.397′*	*2*	*23.22 ± 0.0161*	*0.386 ± 0.01*	*12.17 ± 0.30*	*21.7 ± 0.5*
OBN-05-123-1	1412	84° 47.176′	116° 27.584′	2.5	106.80 ± 0.0091	0.22 ± 0.00	31.27 ± 0.37	56.2 ± 0.7
OBN-05-123-2	1412	84° 47.176′	116° 27.584′	2	10.03 ± 0.0078	3.21 ± 0.06	44.49 ± 0.78	79.3 ± 1.4
OBN-05-135-1	1402	84° 47.17′	116° 27,649′	3	8.78 ± 0.0005	5.22 ± 0.06	63.31 ± 0.76	115.7 ± 1.4
OBN-05-136-1	1402	84° 47.17′	116° 27,649′	2	3.74 ± 0.0004	5.38 ± 0.09	27.83 ± 0.45	50.0 ± 0.8
OBN-05-136-2	1402	84° 47.17′	116° 27,649′	2	6.73 ± 0.0003	3.04 ± 0.05	28.19 ± 0.43	50.6 ± 0.8
OBN-05-136-3	1402	84° 47.17′	116° 27,649′	2	7.88 ± 0.0047	2.62 ± 0.06	28.52 ± 0.61	51.2 ± 1.1
OBN-05-136							*Mean*	50.5 ± 0.5
OBN-05-203-1	1421	84° 47.272′	116° 23.656′	2.5	23.94 ± 0.0044	1.53 ± 0.06	50.39 ± 1.91	89.9 ± 3.4
OBN-05-203-2	1421	84° 47.272′	116° 23.656′	2.5	19.15 ± 0.0012	1.95 ± 0.06	51.43 ± 1.56	91.8 ± 2.8
OBN-05-203							*Mean*	91.0 ± 2.2
OBN-05-204-1	1409	84° 47.174′	116° 27.624′	3	2.31 ± 0.0003	3.32 ± 0.08	10.60 ± 0.24	*19.5* ± 0.4
OBN-05-205-1	1408	84° 47.174′	116° 27.624′	2.5	16.98 ± 0.0020	0.85 ± 0.02	19.77 ± 0.42	35.6 ± *0.8*
OBN-05-210-1	1415	84° 47.192′	116° 27.518′	2.5	6.88 ± 0.0004	9.22 ± 0.11	87.64 ± 1.07	157.1 ± 1.9
OBN-05-211-1	1402	84° 47.17′	116° 27.649′	2.5	6.49 ± 0.0004	1.49 ± 0.03	13.33 ± 0.27	24.1 ± 0.5
OBN-05-211-2	*1402*	*84° 47.17′*	*116° 27.649′*	*2.5*	*4.54 ± 0.0032*	*2.77 ± 0.06*	*17.38 ± 0.39*	*31.5* ± 0.7
Darling Ridge								
ODR-05-030A-1	1665	84° 45.093′	115° 47.667′	2.5	2.28 ± 0.0002	2.85 ± 0.07	8.96 ± 0.21	14.2 ± 0.3
ODR-05-030B-1	1665	84° 45.093′	115° 47.667′	2.5	14.55 ± 0.0118	0.35 ± 0.01	6.88 ± 0.23	9.5 ± 0.3
ODR-05-030B-2	1665	84° 45.093′	115° 47.667′	2	26.28 ± 0.0013	0.17 ± 0.00	6.07 ± 0.18	10.9 ± 0.4
ODR-05-030B							*Mean*	10.0 ± 0.2
Discovery Ridge								
ODY-05-014-1	1681	84° 43.646′	114° 13.667′	2	16.81 ± 0.0019	1.51 ± 0.02	34.97 ± 0.52	51.5 ± 0.8
ODY-05-015-1	1682	84° 43.646′	114° 13.667′	2	8.63 ± 0.0004	1.58 ± 0.03	18.77 ± 0.35	27.2 ± 0.5
ODY-05-015-2	1682	84° 43.646′	114° 13.667′	2	8.75 ± 0.0008	1.74 ± 0.03	20.96 ± 0.37	30.4 ± 0.5
ODY-05-015								28.7 ± 0.4
ODY-05-016-1	1682	84° 43.646′	114° 13.667′	3	96.09 ± 0.0210	0.06 ± 0.00	6.76 ± 0.16	*9.9* ± 0.2
ODY-05-016-2	1682	84° 43.646′	114° 13.667′	3	13.42 ± 0.0011	0.40 ± 0.01	7.27 ± 0.19	10.7 ± *0.3*
ODY-05-016								10.3 ± 0.2

Table 1 (*continued*)

Sample	Elevation (m)	Latitude S	Longitude W	Depth (cm)	^{4}He (atom/g × 10^{12})	^{3}He/^{4}He (R/Ra)	^{3}He cosmo (atom/g × 10^6)	Age (ka)
ODY-05-056-1	1681	84° 43.629′	114° 13.76′	2	5.84 ± 0.0004	24.45 ± 0.26	197.65 ± 2.09	290.9 ± 3.1
ODY-05-057-1	1681	84° 43.629′	114° 13.76′	2	12.30 ± 0.0006	18.91 ± 0.19	321.65 ± 3.29	469.4 ± 4.8
ODY-05-058-1	1681	84° 43.629′	114° 13.76′	2	13.94 ± 0.0011	1.21 ± 0.02	23.28 ± 0.44	34.2 ± 0.6
ODY-05-058-2	1681	84° 43.629′	114° 13.76′	2	15.99 ± 0.0008	1.26 ± 0.02	27.84 ± 0.45	40.8 ± 0.7
ODY-05-058							*Mean*	37.5 ± 0.5
ODY-05-059-1	1681	84° 43.629′	114° 13.76′	2	32.18 ± 0.0011	5.25 ± 0.06	233.72 ± 2.51	337.2 ± 3.6
ODY-05-059-2	1681	84° 43.629′	114° 13.76′	2	9.15 ± 0.0006	17.77 ± 0.19	224.97 ± 2.41	324.6 ± 3.5
ODY-05-059-3	1681	84° 43.629′	114° 13.76′	2	19.09 ± 0.0006	8.61 ± 0.09	227.31 ± 2.49	328.0 ± 3.6
ODY-05-059-4	1681	84° 43.629′	114° 13.76′	2	6.15 ± 0.004	25.74 ± 0.35	218.95 ± 2.98	315.9 ± 4.3
ODY-05-059								327.2 ± 1.9
ODY-05-060-1	1676	84° 43.664′	114° 13.102′	2	15.04 ± 0.0011	11.47 ± 0.13	238.83 ± 3.11	*351.8* ± 4.6
ODY-05-114-1	1683	84° 43.639′	114° 13.682′	2	156.30 ± 0.0180	0.54 ± 0.01	115.84 ± 3.03	168.3 ± *4.4*
ODY-05-114-2	1683	84° 43.639′	114° 13.682′	2	29.98 ± 0.0018	2.92 ± 0.06	121.13 ± 2.48	176.0 ± 3.6
ODY-05-114							*Mean*	172.9 ± 2.8
Discovery Ridge ice-cored moraine								
OTB-05-002-1	1573	84° 43.991′	114° 17.873′	2.5	38.91 ± 0.0063	0.56 ± 0.02	29.97 ± 1.25	*47.4* ± 2.0
OTB-05-002-2	1573	84° 43.991′	114° 17.873′	2.5	10.70 ± 0.0006	2.06 ± 0.09	30.46 ± 1.35	48.2 ± *2.1*
OTB-05-002							*Mean*	47.8 ± 1.5
OTB-05-003-1	1563	84° 44.001′	114° 17.714′	1.5	8.61 ± 0.0006	7.33 ± 0.17	87.32 ± 2.07	*136.9* ± 3.2
OTB-05-004-1	1562	84° 44.001′	114° 17.714′	3	13.55 ± 0.0009	1.73 ± 0.03	32.29 ± 0.54	52.0 ± *0.9*
OTB-05-052-1	1572	84° 44.005′	114° 17.606′	1	44.56 ± 0.0032	1.48 ± 0.02	90.88 ± 1.08	140.3 ± 1.7
OTB-05-102-1	1571	84° 43.985′	114° 17.94′	2.5	34.11 ± 0.0051	1.67 ± 0.05	78.57 ± 2.26	124.5 ± 3.6
OTB-05-102-2	1571	84° 43.985′	114° 17.94′	2.5	23.18 ± 0.0014	2.37 ± 0.07	75.95 ± 2.09	120.3 ± 3.3
OTB-05-102							*Mean*	122.2 ± 2.4
OTB-05-103-1	1563	84° 44.001′	114° 17.666′	2.5	1153.99 ± 0.0833	0.04 ± 0.00	52.33 ± 0.84	*83.4* ± 1.3
OTB-05-112	1561	84° 43.695′	114° 21.772′	2.5	28.32 ± 0.0030	0.76 ± 0.01	29.43 ± 0.56	47.0 ± *0.9*
OTB-05-113	1557	84° 43.592′	114° 21.746′	2.5	4.03 ± 0.0005	8.29 ± 0.14	46.21 ± 0.77	74.0 ± 1.2
Darling Ridge ice-cored moraine, West								
ODR-05-007-1	1378	84° 45.737′	116° 6.491′	2	17.87 ± 0.0012	0.17 ± 0.01	4.10 ± 0.17	7.5 ± 0.3
ODR-05-008-1	1378	84° 45.737′	116° 6.491′	2.5	43.92 ± 0.0031	0.09 ± 0.00	5.12 ± 0.19	9.5 ± 0.3
ODR-05-009-1	1378	84° 45.737′	116° 6.491′	2.5	45.03 ± 0.0048	0.27 ± 0.01	16.34 ± 0.38	30.2 ± 0.7
ODR-05-107-1	1385	84° 45.685′	116° 6.275′	2.5	17.70 ± 0.002	0.13 ± 0.01	3.03 ± 0.18	5.6 ± 0.3
ODR-05-108-1	1385	84° 45.697′	116° 6.221′	2.5	21.52 ± 0.002	0.20 ± 0.00	5.89 ± 0.11	10.8 ± 0.2
Darling Ridge ice-cored moraine, East								
ODR-05-111-1	1377	84° 45.645′	116° 6.389′	2.5	17.15 ± 0.0172	1.69 ± 0.03	39.88 ± 0.67	73.7 ± 1.2
ODR-05-128-1	1468	84° 44.837′	115° 50.172′	2.5	128.66 ± 0.0137	0.20 ± 0.00	35.04 ± 0.62	60.2 ± 1.1
ODR-05-129-1	1468	84° 44.837′	115° 50.172′	2.5	56.88 ± 0.0066	0.29 ± 0.01	22.04 ± 0.45	37.9 ± 0.8
ODR-05-130-1	1468	84° 44.837′	115° 50.172′	2.5	48.38 ± 0.0054	0.58 ± 0.01	38.54 ± 0.65	66.2 ± 1.1

Helium was extracted by melting quartz separates from granite clasts. Means or the highest value of replicate analyses are in italics. Helium in samples ending in a or b was extracted in two steps; total ^{3}He is the sum of *a* and *b*. The production rate of 126 atoms/g/yr was obtained by scaling the production rate in olivine (120 ± 9.4 atoms/g/yr; Goehring et al., 2010) to quartz using elemental production rates (Masarik and Reedy, 1996). Scaling after Stone (2000). Errors are for analytical uncertainties only; ages do not include production rate uncertainties. R/Ra is the atmospheric ^{3}He/^{4}He = 1.384 × 10^{-6}.

Table 2
^{3}He and ^{10}Be exposure ages of granite erratics from the Ohio Range.

	Elevation (m)	^{3}He (atoms/g × 10^6)	^{3}He Age (ka)	^{10}Be (atoms/g × 10^6)	^{10}Be Age (ka)
Discovery Ridge					
ODY-05-014	1680	34.97 ± 0.52	51.9 ± 4.1	1.82 ± 0.04	74.3 ± 6.8
ODY-05-015	1680	18.77 ± 0.35	28.7 ± 1.6	0.89 ± 0.03	35.8 ± 3.4
ODY-05-016	*1680*	*6.76 ± 0.16*	*10.3 ± 0.6*	*0.26 ± 0.01*	*10.8 ± 1.0*
ODY-05-056	1680	197.65 ± 2.09	290.9 ± 23.0	9.25 ± 0.27	411.0 ± 42.0
ODY-05-057	1680	321.65 ± 3.29	469.4 ± 37.2	13.17 ± 0.42	616.7 ± 67.1
Darling Ridge					
ODR-05-030A	1665	8.96 ± 0.21	14.2 ± 1.2	0.80 ± 0.03	35.3 ± 3.4
ODR-05-030B	*1665*	*6.07 ± 0.18*	*10.0 ± 0.6*	*0.30 ± 0.01*	*12.9 ± 1.3*
Bennett Nunataks					
OBN-05-025	1465	64.26 ± 0.96	111.7 ± 8.8	2.81 ± 0.06	138.6 ± 12.8
OBN-05-122	1410	9.45 ± 0.24	21.7 ± 1.8	1.82 ± 0.09	91.9 ± 9.4
OBN-05-136	1415	28.01 ± 0.25	50.5 ± 2.4	1.46 ± 1.46	73.1 ± 6.8
OBN-05-204	1415	10.60 ± 0.24	19.5 ± 1.6	0.52 ± 0.02	26.3 ± 2.5
OBN-05-211	1415	13.33 ± 0.27	31.5 ± 2.6	1.60 ± 0.05	80.8 ± 7.6
Tuning Nunatak					
OTN-05-019	1540	28.74 ± 0.35	46.7 ± 2.2	1.68 ± 0.04	77.5 ± 7.1
OTN-05-120	1515	1.17 ± 0.02	44.7 ± 2.8	1.44 ± 0.04	67.6 ± 6.3

Production rate (SLHL) in Quartz for ^{3}He is 125 ± 9 atoms/g/yr; See Table 1: for ^{10}Be is 4.49 ± 0.39 atoms/g/yr with a decay constant of 5.1 × 10^{-7} (Balco et al., 2008). Altitude scaling is after Stone (2000). Ages include production rate uncertainties, with erosion rate = 0. ^{10}Be ages are calculated using Cronus calculator (Balco et al., 2008). Latitude, longitude, shielding and thickness of samples are in Table 1. Data in italics is from Ackert et al., 2007.

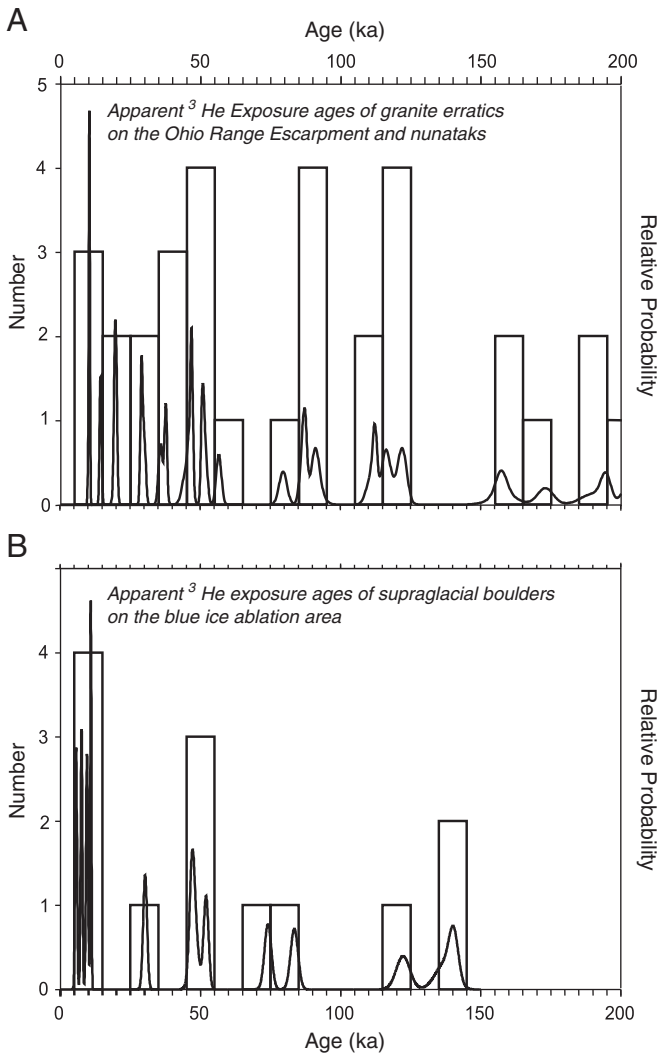

Fig. 3. A) Histogram and probability density function (PDF) of ^{3}He exposure ages (n = 32) from granite erratics on the Ohio Range Escarpment and nearby nunataks. B) Histogram and PDF of ^{3}He exposure ages (n = 13) of granite boulders from ice-cored moraines on the WAIS surface at the Ohio Range.

the same direction while random errors will tend to degrade the peaks. Thus, while there is ~10% uncertainty in the actual position (age) of the peaks in the PDF, the existence of the peaks is a robust finding. The exposure ages of erratics from the escarpment and nunataks are shown in Fig. 3A. The exposure ages cluster in four groups, with distinct peaks centered on 50 ka, 90 ka and 120 ka. We conclude that the apparent ^{3}He exposure age distribution is not random, and suggest that peaks and gaps in the exposure age distribution relate to past WAIS fluctuations.

Fig. 3B shows the distribution of apparent ^{3}He exposure ages of clasts from the WAIS surface. The range of exposure ages, with a peak centered on 50 ka, is similar to that of the erratics (Fig. 3A). Notable differences between the distributions are the occurrence of younger exposure ages on the WAIS surface near Darling Ridge and the apparent lack of ^{3}He exposure ages older than 140 ka. Younger ages are expected on the ice surface where debris continues to accumulate while deposition of erratics at a given elevation stops once the ice level drops below it. The lack of older exposure ages on the ice surface may simply be the result of the relatively small number of samples of ice-cored debris. The presence of the 50 ka peak in both exposure age distributions with a similar range of ages (Fig. 3A and B) supports the inference that the erratics and boulders from the ice-cored moraines on the WAIS surface are derived from the same source.

3.2. Equivalent ^{10}Be ages

The relationship between the measured ^{3}He and ^{10}Be concentrations in quartz is remarkably strong given that ^{3}He is subject to diffusion and ^{10}Be to radioactive decay (Fig. 4). The best fit to the data was obtained using a quadratic equation constrained to go through the origin ($R^2 = 0.99$). This equation was used to calculate "equivalent ^{10}Be concentrations" from the measured ^{3}He concentrations for the samples lacking ^{10}Be measurements, which were in turn used to calculate "equivalent ^{10}Be exposure ages." The uncertainties in the equivalent ^{10}Be concentrations were calculated by propagating the ^{3}He uncertainty with the uncertainty in the coefficients of the quadratic regression. There are two outliers that fall significantly off the trend line such that their equivalent ^{10}Be ages differ significantly from their actual ^{10}Be ages. It is conceivable that a similar proportion (~15%) of the equivalent ^{10}Be ages that we compute from the ^{3}He data are similarly in error, but note that these errors would tend to degrade rather than enhance the clustering of exposure ages. The PDF and histogram of the equivalent ^{10}Be exposure ages, including both erratics and ice-cored debris appears in Fig. 5, which illustrates that the exposure ages are clustered with peaks centered at 12 ka, 75 ka, 135 ka and 180 ka.

4. Evidence for supraglacial exposure of boulders in the blue ice ablation areas

In this section, we discuss processes and mechanisms that could potentially produce the observed exposure age distribution at the Ohio Range. We conclude that significant exposure of boulders occurs on the WAIS surface, prior to deposition on the escarpment and nunataks.

4.1. Are the older exposure ages, or clustering of exposure ages, related to prior exposure in the bedrock?

The clusters of pre-LGM exposure ages may be related to WAIS fluctuations or to variable amounts of exposure of bedrock prior to incorporation into the glacial system. We retain the phrase "prior exposure" as traditionally used, to differentiate this type of exposure from that which occurs after deposition into the glacial system. Many of the boulders in the Ohio Range exhibit clearly weathered surfaces on one or more faces. Those rocks most likely were incorporated into the WAIS by mass wasting from outcrops along the escarpment and presumably have significantly older apparent exposure ages. Boulders exhibiting these characteristics were not sampled. ^{21}Ne and ^{10}Be exposure ages from bedrock surfaces on the escarpment and nunataks indicate they are older than 3.5 Ma and (manuscript in preparation).

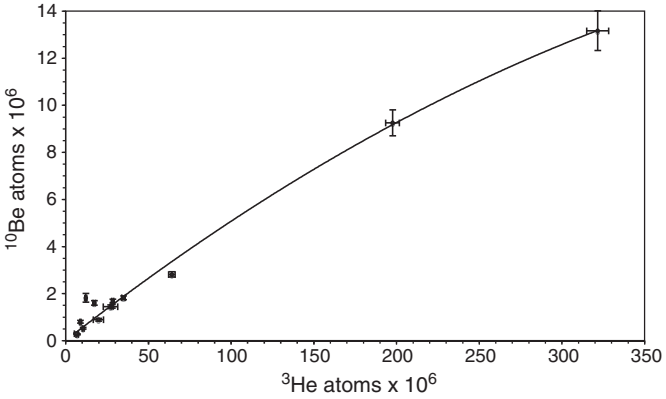

Fig. 4. Plot of ^{3}He atoms/g vs. ^{10}Be atoms/g. The best fit curve $y = -0.000044x^2 + 0.055x$ is used to calculate "equivalent ^{10}Be concentrations".

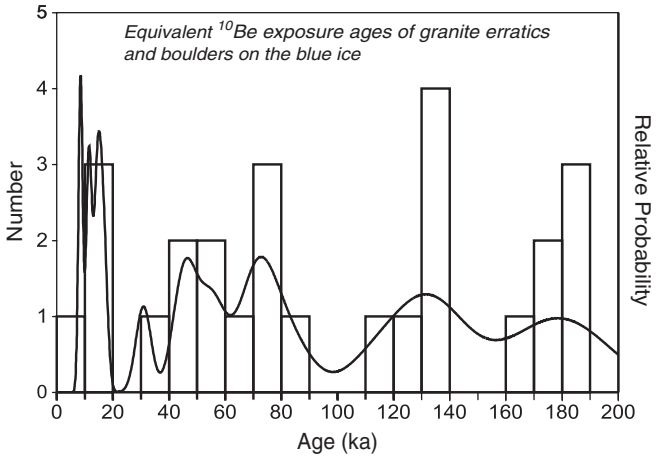

Fig. 5. Histogram and PDF (n = 38) of equivalent ^{10}Be ages determined from a quadratic relationship between ^{3}He and ^{10}Be ages of granite erratics on the Ohio Range Escarpment and nearby nunataks (See Fig. 4). The PDF includes analytical uncertainties, uncertainties in the coefficients of the quadratic fit, and production rate uncertainties.

Thus, material sourced from such surfaces would have exposure ages much greater than we observe in the sampled erratics and ice-cored moraine boulders.

It is conceivable that our samples could be sourced from some depth below these old weathered surfaces because production rates decrease exponentially with depth. For bedrock surfaces with millions of years of exposure, cosmogenic nuclide concentrations within the upper 1–2 m would be comparable to those measured in Ohio Range erratics. However, in order for such a scenario to explain the observed clustering of exposure ages (Fig. 5), rocks from only a few specified depths in the bedrock of the escarpment must have been preferentially incorporated into the glacial system and then collected by us. This seems extremely unlikely.

Therefore, the clustering of the exposure ages argues against pervasive prior exposure. The fact that the youngest cluster of ages 10–20 ka, corresponds to the warming leading to the last highstand shows that for at least those samples, prior exposure must be minimal, on order a few thousand years at most. Most of the samples we collected were probably quarried beneath icefalls on the escarpment where glacial erosion has removed any rock that had prior exposure. We conclude that prior exposure is not a significant factor with the bulk of our samples. The range and clustering of the exposure ages observed in our samples from the Ohio Range must be related to exposure *after* incorporation into the glacial system.

4.2. Does the clustering of exposure ages record earlier fluctuations in WAIS elevation?

Typically, when prior exposure and erosion are negligible, the exposure age of an erratic boulder is interpreted as closely dating the retreat of the ice margin from that location (e.g. Bentley et al., 2010; Mackintosh et al., 2007; Stone et al., 2003). This interpretation is supported when there is a systematic decrease in exposure age with lower elevation. However, older outliers are often observed below the maximum ice elevation. The outliers may record prior exposure, or earlier glacier fluctuations. In Antarctica, cold-based ice margins do not noticeably erode the underlying surfaces and features such as weathered bedrock, boulder belt moraines and erratics commonly survive overriding e.g. (Brook et al., 1993).

However, in the Ohio Range there is not a clear relationship between exposure age and either elevation or position relative to the ice margin. Thus, the clusters of exposure ages cannot be associated with a specific WAIS elevation. Moreover, old exposure ages occur at the elevation of the last highstand at ~10 ka. For example, at Discovery Ridge, a boulder moraine near the edge of a relatively level bench marks the last WAIS highstand (Ackert et al., 2007 and Supplemental Fig. 1). Significantly, no erratics occur either on the bench or the slope beyond the moraine. Moreover, paired ^{21}Ne–^{10}Be exposure ages of the bedrock of the bench indicate millions of years of simple exposure (manuscript in prep), suggesting the WAIS barely overtopped the bench. Fresh-appearing erratics from the bench have ^{10}Be exposure ages ranging from 10.8 ka to 74.3 ka (Table 2). It seems improbable that past WAIS highstands during both the last glaciation and earlier glaciations would consistently reach precisely the same position on the bench. Therefore, it appears erratics with a range of exposure ages were deposited on the Discovery Bench during a single event at ~10 ka.

In contrast, we cannot rule out multiple deposition events on the nunataks that lie below the trimline, where the WAIS may have overtopped the nunataks on multiple occasions. If WAIS elevation during the last interglacial was as low as the present, the nunataks near Darling Ridge must have been over-run by ice during the last glaciation. Similarity in WAIS elevations during the last two interglacials are supported by our ice sheet model (see Section 5.3), which also indicates additional WAIS fluctuations that over topped the nunataks but did not reach the elevation of the last highstand. Erratics deposited during rising ice levels or earlier WAIS fluctuations would be ice covered during the WAIS highstand leading to complex exposure histories and potentially biasing some of the sampled erratics to younger ages. To minimize the problem with ice cover, we focused our sampling on the nunataks peaks where the duration of ice cover would be shortest.

4.3. Supraglacial exposure of boulders in blue ice areas

We suggest that the wide range of exposure ages found along the Ohio Range trimline record exposure of boulders within the blue ice area prior to deposition on the escarpment and nunataks. Unweathered clasts with apparent ^{3}He exposure ages ranging from 7.5 ka to at least 140 ka occur on the WAIS surface today (Table 1; Fig. 3B), with the oldest ages found on the ice-cored moraine below Discovery Ridge. The oldest equivalent ^{10}Be ages are ~200 ka. We infer that significant exposure occurs only after emergence of debris in the blue ice areas. We use the term “supraglacial exposure” to distinguish this exposure from “prior exposure.” The clustering of the exposure ages (Figs. 3 and 5) implies that the flux of unweathered englacial debris to the surface in the blue ice areas is not constant or random, but occurs in pulses.

The presence of boulders on the blue ice with a range of supraglacial exposure ages similar to that of the erratics from the Ohio Range trimline, provides a mechanism whereby boulders with a range of exposure ages could be deposited during a single event. We conclude that the erratics at Discovery and Darling Ridge were deposited at ~10 ka with a range of cosmogenic nuclide concentrations inherited from sequential exposure in the blue ice areas. Thus, the exposure ages of erratics record the combined exposure on the WAIS surface and exposure subsequent to deposition on the escarpment and nunataks.

We note that this process likely occurs at many locations in Antarctica and could explain the presence of older exposure ages in LGM and younger drift observed at some other locations. Moraines and drift commonly occur adjacent to blue ice areas with supraglacial debris and low surface slopes where the ice sheet or lobes of outlet glaciers flow into ice-free tributary valleys.

4.4. The limited role of boulder reorientation and ice cover on exposure ages

Given that the inferred exposure history of the erratics includes both supraglacial exposure on the ice surface and subsequent transfer to ice-free terrain, the clustering of the exposure ages is surprising. Typically, at active glacier margins, frequent reorientation of boulders occurs on the ice and during deposition as differential melting and slumping occurs. The accompanying variations in in situ production

rates would normally be expected to lead to a more random distribution of apparent exposure ages. However, reorientation of boulders has not erased the clustering of surface exposure ages that we observe at the Ohio Range. This may be due to the low slope of the blue ice surface, limiting the potential for boulder slumping. Numerous perched boulders attest to the delicacy of the depositional process (Supplemental Fig. 2). Evidently, clasts are lowered vertically on to the underlying bedrock or boulders as the ice sublimates.

A perhaps more important factor is that smaller erratic boulders, often <10 cm thick, were typically collected because larger, unweathered erratics are rare in the Ohio Range. Such thin samples have relatively uniform cosmogenic isotope concentrations (<10% difference between tops and bottoms assuming 2 cm average sample depth) so that reorientation does not significantly change in situ production rates.

4.5. Interpretation of the peaks in the exposure age distribution

The PDF of the combined equivalent ^{10}Be exposure ages of erratics from the escarpment, nunataks and ice-cored moraines (Fig. 5) shows distinct clusters that we interpret as evidence for changes in the debris flux into the blue ice areas. As we have shown, complex exposure and other processes that introduce scatter in the exposure age distribution are limited and the surface exposure ages include both initial exposure on the blue ice and subsequent exposure after deposition on adjacent ice-free terrain. It follows that the clusters in the exposure age distribution record pulses (relative increases) in the englacial debris flux into the blue ice areas at ~12, ~75, ~135, and ~180 ka. Some of this debris was eventually deposited on the escarpment and nunataks, but the greater part remains on the WAIS surface in the blue ice areas.

5. Discussion

We now discuss the implications of the geologic observations and the exposure age distribution for WAIS dynamics. In order to investigate the possible relationship of debris pulses to WAIS elevation changes, we compare the PDF and histogram of the exposure age distribution to an ice core temperature record and an ice sheet model. We acknowledge that observed relationships between debris pulses and paleoclimate records, or between debris pulses and simulated ice dynamics, may be complicated by sampling bias (Section 2.1), random errors (Section 4.5), and errors in calculating the exposure ages (Section 3.2). For example, the exposure age uncertainties at ~120 ka are possibly as high as ±12 ka, which is sufficient to switch the timing of debris pulse centered at 135 ka from warming temperatures (rising ice levels) to cooling (decreasing ice levels), i.e. to the penultimate glacial maximum. While this scenario cannot be ruled out, large systematic offsets would not change the correlation between the most recent (10–20 ka) debris pulse and warming at the last glacial termination. Therefore, we hypothesize that the peaks in exposure ages are linked in some systematic way to ice dynamics. We investigate this possibility below, mindful that firm conclusions await further investigation using additional samples collected specifically to address this issue, refinement of cosmogenic production rates and direct measurements of ^{10}Be.

5.1. Implications of the exposure age distribution for inferring past WAIS history

The presence of boulders with exposure ages as old as 200 ka on the WAIS surface in the Ohio Range indicates that the blue ice areas have existed continuously for at least that long. If these areas had ever become accumulation zones due to changes in the prevailing winds, ice flow would reverse and the supraglacial material would have been carried away into the WAIS. Similarly, if WAIS elevations had dropped 100s of meters, ice would have flowed out of the blue ice areas. Therefore, we infer that there was no significant change in the local ice flow (or local climate) regime during the peak of the last interglacial (isotope stage 5e). It has long been speculated that the WAIS may have collapsed during this interval raising sea level by ~5 m (Mercer, 1978). The old exposure ages of supraglacial debris in the Ohio Range thus place some constraints on WAIS behavior during this key interval. As discussed below (Section 5.3), these data argue against complete WAIS collapse. We use the phrase "complete WAIS collapse" to refer to disappearance of both ice grounded below and above present day sea level (i.e. loss of ice volume equivalent to ~5 m of global sea level).

We hypothesize that the debris pulses in the Ohio Range are linked to WAIS elevation changes and associated changes in ice dynamics. For example, debris pulses could result from increased subglacial erosion under thicker ice, resulting in higher englacial debris concentration. Alternatively, if the input of debris were relatively constant, higher ice flux into the ablation area, higher ablation rates, or a combination of the above factors, would result in debris pulses. Possible linkages include warmer temperatures that would both increase accumulation rates and hence regional ice elevations, as well as, ablation rates and ice (debris) flux into the blue ice areas.

5.2. Comparison of the exposure age distribution with the Dome Fuji ice core record

The Dome Fuji Ice Core (Kawamura et al., 2007) in East Antarctica (Fig. 1A) is the nearest ice core with a record that spans the last 200 ka. The δ^{18}O of ice is a proxy for surface air temperature at the core site (Fig. 6A). The Dome Fuji δ^{18}O record is very similar to that of the Byrd Core (Johnsen et al., 1972) in West Antarctica (Fig. 1A) on the opposite side of the Ohio Range, indicating similar climatic conditions existed across interior West Antarctica and that the Dome Fuji temperature record is representative of conditions in the Ohio Range. The Dome Fuji δ^{18}O record is characterized by Milankovitch period oscillations with superimposed millennial scale fluctuations. Peak temperatures occur at the end of terminations, the abrupt rises in temperature following maximum glacial conditions at ~18 ka and at ~140 ka.

There is a general correspondence between peaks in the exposure age distribution (Fig. 6C) and warming temperatures (lighter δ^{18}O; Fig. 6A) with peaks in the exposure age distribution corresponding to peaks in δ^{18}O at 10, 80, 130 and at ~180 ka. In detail, two of the peaks in the exposure ages occur during the abrupt and largest rises in temperature preceding the last two interglacials, between10–20 ka and 130–140 ka. The oldest peak at ~180 ka occurs during an abrupt but much smaller warming. In contrast, the peak at 70–80 ka occurs during an interval of falling temperatures and post-dates peak warmth by around 5–10 ka. This peak occurs within a plateau in the exposure age distribution slightly above the background level beginning 30 ka and ending at 70 ka that corresponds to both warm and cool periods. Additionally, there is no peak in exposure ages corresponding to the warming 115 to 105 ka. This may be a real feature of the record or may represent a statistical artifact related to the sampling of relative small number of boulders and erratics and our bias toward sampling younger samples.

5.3. Comparison of the exposure age distribution with an ice sheet model

In order to more directly compare the glacial geologic record and exposure age distribution to WAIS fluctuations, we utilize a combined ice sheet/ice shelf model that predicts WAIS behavior over the last 5 Ma (Pollard and DeConto, 2009). The model uses scaled dynamical equations for sheet and shelf flow depending on whether the ice is grounded or floating. Mass flux across the grounding line between the two domains is a function of ice thickness (Schoof, 2007) and incorporates the effects of ice shelf buttressing. Modern parameterizations of temperature and precipitation are scaled to marine δ^{18}O and the

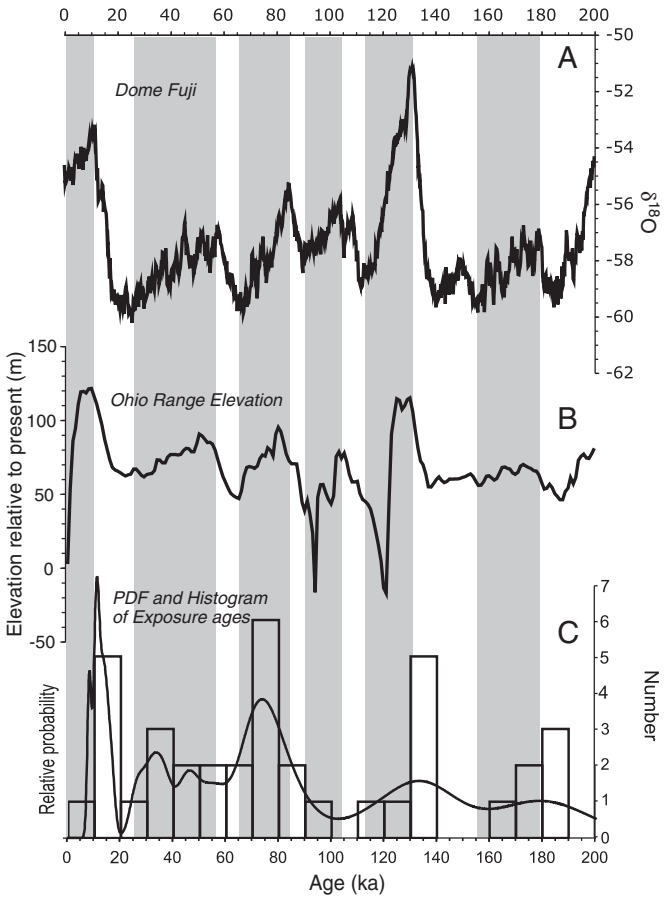

Fig. 6. A) The $\delta^{18}O$ from the Dome Fuji Ice core in East Antarctica (Fig. 1A). The $\delta^{18}O$ is a proxy for air temperature at the core site with less negative values corresponding to warmer temperatures. B) Simulated elevation changes at the Ohio Range from an ice sheet model. C) Histogram and probability density function (PDF) of combined ^{10}Be ages and equivalent ^{10}Be exposure ages of erratics and boulders on the WAIS surface in the Ohio Range. The uncertainties in the PDF are as in Fig. 5.

annual 80° S insolation anomaly. Sub-ice-shelf melting is parameterized based on the degree of protection by islands and bays and distance to the ice shelf edge.

Fig. 6B shows the simulated elevation history for the last 200 ka at the nearest model grid point to the Ohio Range from a more recent model simulation of the last 400 ka, in which basal sliding coefficients were increased under WAIS by a factor of ten in order to better match modern and LGM ice elevations in the Siple Coast region. This model is very similar to that described in the Supplementary information, Section 7 of Pollard and Deconto (2009), where the effects on WAIS volume and surface elevations for higher basal slip are shown and where the differences between the higher basal slip model and the nominal (lower basal slip) model are discussed. While the match to interior WAIS elevations is considerably improved in this model compared to the nominal model, the simulated elevations near the Ohio Range are still several hundred meters higher than observed, a problem common to other models (Ackert et al., 2007). However, the timing and magnitude of the simulated elevation changes in the two models are similar, indicating that the relative changes in WAIS elevation are more robust.

The timing of the simulated elevation changes correlates well with the Dome Fuji $\delta^{18}O$ (surface temperature) record ($R=0.51$; $P<0.001$), consistent with higher interior WAIS elevations primarily resulting from enhanced accumulation accompanying peak temperatures. However, the role of ice dynamics is also evident. Rapid down-draw events at 95 ka and 120 ka reflect the arrival of a wave of thinning propagating inland following significant retreat of the grounding line. The relative highstands between 30 ka and 90 ka lag peak temperatures by ~5 ka.

The simulated elevation changes vary ~125 m over the last glacial cycle with maximum ice elevation reached ~10 ka in excellent agreement with the geologic data. As geologic constraints on interior WAIS ice elevation (Ackert et al., 1999, 2007) were not used to tune the model, this result provides independent verification of the ice sheet model. In addition, the simulated interglacial highstand elevations at the Ohio Range increase over the last 400 ka peaking at 10 ka. This also agrees with observations in the Ohio Range that no evidence of higher WAIS elevations exists above the trimline of the last highstand. The timing of the penultimate highstand in the model simulation occurs early in the last interglacial, similar to the observations of last highstand. Earlier relative high stands occur at ~50 ka, ~80 ka and 110 ka with average WAIS elevations between 50 m and 80 m above present. The model's skill in reproducing the recent ice sheet history in the Ohio Range indicates that the ice sheet/ice shelf model captures interior as well as peripheral WAIS dynamics.

Given the good correlation between the simulated elevation history and the ice core temperature record, it is not surprising that the peaks in the exposure age distribution at 10–20 ka and 130–140 ka correspond to the rapid elevation increases leading to the last two WAIS highstands. Debris pulses during these intervals could be the result of higher local ablation rates associated with maximum temperatures and increased ice (debris) flux into the local ablation areas as the regional WAIS surface rises.

Since ice elevation lags relative to temperature, the peak in exposure ages 70–80 ka shows better correspondence with modeled WAIS elevation than to temperature, but the peak clearly does not occur during the rapid elevation rise/temperature increase, as is the case during the terminations. Erratics with exposure ages comprising this peak are predominately from the nunataks that must have been ice-covered during the last highstand. The simulated elevation history indicates 5–10 ka of ice cover would occur between 5 and 15 ka, which would, when added to the exposure ages, be sufficient to move the actual timing of the debris pulse to abrupt warming at 80–90 ka.

The simulated WAIS history indicates ice elevation at the Ohio Range (Fig. 6B) during the last interglacial was similar to the present, consistent with observations of exposure ages up to 200 ka in the supraglacial debris that attest to the long term stability of the WAIS at the Ohio Range. However, the model simulates overall Antarctic Ice Sheet extent and ice volume during the last interglacial (stage 5e) to be similar to the present, suggesting WAIS collapse does not occur during isotope stage 5e. Collapse of the marine portion of the WAIS (grounded below present day sea level) does occur in the model simulation during some earlier interglacials (Pollard and DeConto, 2009, SI Fig. 7). While the total number of collapses in the simulation is reasonable, their imprecise timing is an aspect of the model that requires further refinement (Pollard and DeConto, 2009).

Global sea level during stage 5e was at least 6 m higher than the present day with at least 2.5 of that increase attributed to a decrease in WAIS volume (Kopp et al., 2009). In this regard, the geologic evidence for WAIS stability around the Ohio Range Escarpment should not be counted as evidence that the WAIS volume was not smaller during stage 5e. Areas such as Marie Byrd Land, the Antarctic Peninsula and between the Ellsworth, Whitmoor and Thiel Mountains, where the regional bedrock is above present day sea level are likely to remain glaciated even when marine portions of the ice sheet disappear (Bamber et al., 2009; Mercer, 1978). In fact, in our model simulations, the Ohio Range remains glaciated with ice elevations only ~100 m below present during collapse of the marine portions of the WAIS. Thus, the geologic evidence combined with the ice sheet model suggests that complete collapse of the WAIS did not occur during stage 5e.

However, collapse of the marine portion of the WAIS during stage 5e remains a possibility. The WAIS contribution to global sea level resulting from removal of the marine portions is ~2.46 m (Bamber et al., 2009).

Thinning of the remaining grounded ice, due to re-equilibration with the new grounding line positions contributes an additional ~0.54 m of sea level with ice elevations in the vicinity of the Ohio Range predicted to be ~100 m below present (Bamber et al., 2009, Fig. S4). The ~3 m contribution to global sea level and the ~100 m elevation changes at the Ohio Range during collapse of the marine portion of the WAIS are also consistent with our model simulations. Thus, while ~5 m of sea level equivalent is currently locked up in the entire WAIS, the geologic evidence for ice stability at the Ohio Range, combined with ice sheet modeling, indicates that WAIS contribution to higher sea level during stage 5e was limited to ~3 m, consistent with independent estimates by Kopp et al. (2009).

The occurrence of maximum interior WAIS elevations following glacial terminations appears to be a robust feature in the ice sheet model, and is consistent with the geologic evidence from the Ohio Range. It is somewhat surprising that an ice sheet model with forcing dominated by marine $\delta^{18}O$, which is an essentially Northern Hemisphere climate signal, would capture temperature-driven elevation changes in interior West Antarctica, given that solar insolation is anti-phased at the precession periodicity. However, the good correspondence of the model results and geologic evidence suggests that the use of marine $\delta^{18}O$ forcing is justified. A possible reason is that the duration of Southern Hemisphere summer, which co-varies with Northern Hemisphere insolation intensity, likely controls Antarctic annual temperatures (Huybers and Denton, 2008). Because the insolation/summer duration driven anomalies occur on a background of global CO_2-driven temperature variation, the warmest temperatures, highest accumulation rates and hence, highest interior WAIS elevations occur at onset of interglacials, prior to down draw or collapse driven by the retreating grounding line.

6. Conclusions

In spite of ^{3}He diffusion in quartz, cosmogenic ^{3}He can be used to efficiently screen for prior exposure and can be calibrated in reference to ^{10}Be to determine surface exposure ages in Antarctica. We infer that the exposure ages of glacial boulders at the Ohio Range record both the exposure at the site where the samples were collected and/or exposure on adjacent blue ice areas, with peaks in the exposure age distribution interpreted as pulses of debris emergence in the blue ice areas. The ages of two of the debris pulses correspond to the abrupt and large increases in surface temperature preceding the last two interglacials.

The WAIS elevation history inferred from geologic observations and the distribution of exposure ages at the Ohio Range provides an independent test of the Pollard and DeConto (2009) ice sheet model over the last 200 ka. The good correspondence between simulated WAIS elevation changes and geologic data suggests that the model accurately captures interior WAIS dynamics. The model indicates that WAIS elevation changes near the Ohio Range were limited to ~125 m with the highest ice elevation occurring at ~10 ka, in excellent agreement with geologic observations. Simulated relative WAIS high stands are also occur at 50 and 80 ka, with the penultimate highstand occurring at 120–130 ka. The occurrence of supra-glacial debris with exposure ages as old as 200 ka indicates local ice flow and WAIS elevations in the Ohio Range did not change dramatically during the last interglacial. This observation, combined with ice sheet model results, suggests that WAIS contribution to higher sea level during stage 5e was limited to ~3 m.

Supplementary materials related to this article can be found online at doi:10.1016/j.epsl.2011.04.015.

Acknowledgements

The authors acknowledge logistical support from Raytheon Polar Services, Air National Guard, and Ken Borak Air. SM and RP specially acknowledge the help and support from Peter Braddock during fieldwork in the Ohio Range and helpful discussions with Peter Huybers. This project was funded by OPP grant 0338271 to SM and 0338189 to HB.

References

Ackert Jr., R.P., Barclay, D.J., Borns Jr., H.W., Calkin, P.E., Kurz, M.D., Steig, E.J., Fastook, J.L., 1999. Measurement of ice sheet elevations in interior West Antarctica. Science 286, 276–280.

Ackert Jr., R.P., Mukhopadhyay, S., Parizek, B.R., Borns, H.W., 2007. Ice elevation near the West Antarctic Ice Sheet Divide during the Last Glaciation. Geophys. Res. Lett. 34, L21506.

Alley, R.B., Whillans, I.M., 1984. Response of the East Antarctica ice sheet to sea-level rise. J. Geophys. Res. 89, 6487–6493.

Anderson, J.B., Shipp, S.S., Lowe, A.L., Wellner, J.S., Mosola, A.B., 2002. The Antarctic Ice Sheet during the Last Glacial Maximum and its subsequent retreat history; a review. Quat. Sci. Rev. 21, 49–70.

Balco, G., Stone, J., Lifton, N., Dunai, T., 2008. A complete and easily accessible means of calculating surface exposure ages or erosion rates from ^{10}Be and ^{26}Al measurements. Quat. Geochronol. 3, 174–195.

Balco, G., Briner, J., Finkel, R., Rayburn, J.A., Ridge, J.C., Schaefer, J.M., 2009. Regional beryllium-10 production rate calibration for the late-glacial northeastern North America. Quat. Geochronol. 4, 93–107.

Bamber, J.L., Riva, R.E.M., Vermeersen, B.L.A., LeBrocq, A.M., 2009. Reassessment of the potential sea-level rise from a collapse of the West Antarctic Ice Sheet. Science 324, 901–903.

Bentley, M.J., Fogwell, C.J., LeBrocq, A.M., Hubbard, A.L., Sugden, D.E., Dunai, T., Freeman, S.P.H.T., 2010. Deglacial history of the West Antarctic Ice Sheet in the Weddell Sea embayment: constraints on past ice volume change. Geology 38, 411–414.

Brambati, A., Corradi, N., Finnocchario, F., Giglio, F., 2002. The position of the Last Glacial Maximum Grounding line in the Joides Basin: an interpretation based on sedimentological and geotechnical data. Bull. R. Soc. NZ 35, 365–372.

Brook, E.J., Kurz, M.D., 1993. Surface-exposure chronology using *in situ* cosmogenic ^{3}He in Antarctic quartz sandstone boulders. Quat. Res. 39, 1–10.

Brook, E.J., Kurz, M.D., Ackert Jr., R.P., Denton, G.H., Brown, E.T., Raisbeck, G.M., Yiou, F., 1993. Chronology of Taylor Glacier advances in Arena Valley, Antarctica, using *in situ* cosmogenic ^{3}He and ^{10}Be. Quat. Res. 39, 11–23.

Brook, E.J., Kurz, M.D., Ackert Jr., R.P., Raisbeck, G., Yiou, F., 1995. Cosmogenic nuclide exposure ages and glacial history of late Quaternary Ross Sea Drift in McMurdo Sound, Antarctica. Earth Planet. Sci. Lett. 131, 41–56.

Goehring, B.M., Kurz, M.D., Balco, G., Schaefer, J.M., Licciardi, J., Lifton, N., 2010. A reevaluation of in situ cosmogenic ^{3}He production rates. Quat. Geochronol. 5, 410–418.

Goehring, B.M., 2006. ^{10}Be exposure ages of erratic boulders in Southern Norway and implications for the history of the Fennoscandian Ice Sheet. M.S. thesis, Oregon State University, Corvallis.

Huybers, P., Denton, G.H., 2008. Antarctic temperature at orbital timescales controlled by summer duration. Nat. Geosci. 1, 787–792.

Johnsen, S.J., Dansgaard, W., Clausen, H.B., Langway, C.C.J., 1972. Oxygen isotope profiles through the Antarctic and Greenland ice sheets. Nature 235, 429–434.

Kawamura, K., Parrenin, F., Lisiecki, L., Uemura, R., Vimeux, F., Severinghaus, J.P., Hutterli, M.A., Nakazawa, T., Aoki, S., Jouzel, J., Raymo, M.E., Matsumoto, K., Nakata, H., Motoyama, H., Fujita, S., Goto-Azuma, K., Fujii, Y., Watanabe, O., 2007. Northern Hemisphere forcing of climatic cycles in Antarctica over the past 360,000 years. Nature 488, 912–916.

Kopp, R.E., Simons, F.J., Mitrovica, J.X., Maloof, A.C., Oppenheimer, M., 2009. Probabilistic assessment of sea level during the Last Interglacial Stage. Nature 462, 863–867.

Licciardi, J.M., 2000. Alpine glacier and pluvial lake records of late Pleistocene climate variability in the western United States. PhD dissertation, Oregon State University, Corvallis, Oregon.

Licht, K.J., Jennings, A.E., Andrews, J.T., Williams, K.M., 1996. Chronology of late Wisconsin ice retreat from the western Ross Sea, Antarctica. Geology 24, 223–226.

Mackintosh, A., White, D., Fink, D., Gore, D.B., Pickard, J., Fanning, P.C., 2007. Exposure ages from mountain dipsticks in Mac. Robertson Land, East Antarctica, indicate little change in ice thickness since the Last Glacial Maximum. Geology 35, 551–554.

Masarik, J., Reedy, R.C., 1996. Monte Carlo simulation of the in-situ-produced cosmogenic nuclides. Radiocarbon 38, 163.

Mercer, J.H., 1963. Glacial geology of the Ohio Range, Central Horlick Mountains, Antarctica, Institute of Polar Studies. Report no. 8. Ohio State University Research Foundation. 13 pages.

Mercer, J.H., 1978. West Antarctic ice sheet and the CO_2 greenhouse effect: a threat of disaster. Nature 271, 321.

Nishiizumi, K., Imamura, M., Caffee, M., Southon, J., Finkel, R., McAninch, J., 2007. Absolute calibration of ^{10}Be AMS standards. Nucl. Instrum. Methods Phys. Res. B 258, 403–413.

Pollard, D., DeConto, R.M., 2009. Modelling West Antarctic ice sheet growth and collapse through the past five million years. Nature 458, 329–333.

Price, S.F., Comway, H., Waddington, E.D., 2007. Evidence for late Pleistocene thinning of Siple Dome. J. Geophys. Res. 112, F03021.

Putnam, A.E., Schaefer, J.M., Barrell, D.J.A., Vandergoes, M.D., Denton, G.H., Kaplan, M.R., Finkel, R.C., Schwartz, R., Goehring, B.M., Kelley, S.E., 2010. In situ cosmogenic Be-10

production-rate calibration from the Southern Alps, New Zealand. Quat. Geochronol. 5, 392–409.
Schoof, C., 2007. Ice sheet grounding line dynamics: steady states, stability, and hysteresis. J. Geophys. Res. 112, F03S28 doi:10.1029/2006JF000664.
Shipp, S., Anderson, J.B., Domack, E.W., 1999. Late Pleistocene/Holocene Retreat of the West Antarctic Ice-sheet System in the Ross Sea. Geol. Soc. Am. Bull. 111, 1486–1516.
Steig, E.J., Fastook, J.L., Zweck, C., Goodwin, I., Licht, K.L., White, J.W.C., Ackert Jr., R.P., 2001. West Antarctic Ice Sheet elevation changes. In: Alley, R.B.B., Bindschadler, R.A. (Eds.), The West Antarctic Ice Sheet; Behavior and Environment. Antarctic Research Series, 77. American Geophysical Union, Washington D.C., pp. 75–90.
Stone, J.O., 2000. Air pressure and cosmogenic isotope production. J. Geophys. Res. 105, 23753–23759.
Stone, J.O., Balco, G.A., Sugden, D.E., Caffee, M.W., Sass, I.L.S., Cowdrey, S.G., Siddoway, C., 2003. Holocene deglaciation of Marie Byrd Land, West Antarctica. Science 299, 99–102.
Todd, C., Stone, J., Conway, H., Hall, B.R., Bromley, G., 2010. Late Quaternary evolution of Reedy Glacier, Antarctica. Quat. Sci. Rev. 29, 1328–1341.
Waddington, E.D., Conway, H., Steig, E.J., Alley, R.B., Brook, E.J., Taylor, K.C., White, J.W.C., 2005. Decoding the dipstick: thickness of Siple Dome, West Antarctica, at the Last Glacial Maximum. Geology 33, 281–284.